

Chapter 4

Cluster Secondary Ion Mass Spectrometry

Joseph Kozole and Nicholas Winograd

Abstract In principle, secondary ion mass spectrometry (SIMS) molecule-specific imaging has vast implications in biological research where submicrometer spatial resolution, uppermost surface layer sensitivity, and chemically unmodified sample preparation are essential. Yet SIMS imaging using atomic projectiles has been rather ineffective when applied to biological materials. The common pitfalls experienced during these analyses include low secondary ion yields, extensive fragmentation, restricted mass ranges, and the accumulation of significant physical and chemical damage after sample erosion beyond 1 % of the surface molecules. Collectively, these limitations considerably reduce the amount of material available for detection and result in inadequate sensitivity for most applications. In response, polyatomic (cluster) ions have been introduced as an alternate imaging projectile. Cluster ion bombardment has been observed to enhance secondary ion yields, extend the spectral mass range, and decrease the incidence of physical and chemical damage during sample erosion. The projectiles are expected to considerably increase the number of molecules available for analysis and to significantly improve the overall sensitivity. Hence, the objectives of this chapter are to describe the unique physical basis for the improvements observed during polyatomic bombardment and to identify the emerging biological applications made practical by the introduction of cluster projectiles to SIMS.

J. Kozole

Department of Chemistry, Penn State University, 104 Chemistry Building,
University Park, Philadelphia, PA 16802, USA

DuPont, Philadelphia, PA, USA

N. Winograd (✉)

Department of Chemistry, Penn State University, 104 Chemistry Building,
University Park, Philadelphia, PA 16802, USA

e-mail: nxw@psu.edu

4.1 Introduction

Energetic (keV) atomic projectiles were first employed to desorb intact molecules for mass-spectrometric (MS) detection nearly 40 years ago [1]. However, polyatomic ions were not identified as potentially valuable projectiles until 20 years later [2]. Appelhans et al. observed that when compared to the atomic Cs^+ , the cluster SF_6^0 increases secondary ion efficiency and decreases the occurrence of sample damage during SIMS molecule analysis. Similar results were achieved using aromatic hydrocarbons, massive glycerol clusters, inorganic complexes, and SF_5^+ as primary sources shortly thereafter [3–6]. Despite the initial success, polyatomic projectiles were not widely adopted by the SIMS community. The reluctance was credited to a number of device performance issues, which included low beam currents, inadequate beam focusing, and poor source lifetimes [6, 7]. Furthermore, the amount of evidence identifying polyatomic projectiles as better-quality sources for SIMS experiments was not overwhelming [6]. Consequently, cluster ion sources were considered too unreliable for implementation to everyday SIMS applications, and the widespread use of well-established atomic projectiles continued.

The mainstream acceptance of polyatomic projectiles to SIMS did not occur until 10 years after the preliminary observations of Appelhans et al. The breakthrough was initiated by the development of commercially available liquid metal ion (LMIG) sources to produce Au_3^+ and Bi_3^+ and by the marketing of improved gas-phase ion sources to produce C_{60}^+ [8–10]. LMIG technology uses a heated, field-emission tip coated in a eutectic metal alloy (AuGe for Au_n^+ or Bi for Bi_n^+) to extract a mixture of metal cluster ions. The ions are mass-selected and electrostatically aligned and focused to generate a bright, spatially defined metal cluster ion beam. On the other hand, gas-phase ion sources use conventional electron impact strategies to ionize vapor-phase C_{60} . The ions are extracted, mass-filtered, and focused using a sophisticated series of beam-minimizing apertures and electrostatic lenses to obtain an intense, laterally defined C_{60} cluster ion beam. Regardless of scheme, polyatomic ion beam technology has successfully developed high-performance ion sources characterized by 1-nA maximum beam currents, ~100–200-nm optimal beam sizes, and 1,000-h source lifetimes. Consequent to the previously observed enhancements and the aforementioned technical advances, Au_3^+ , Bi_3^+ , and C_{60}^+ cluster projectiles were rapidly adapted to SIMS instrumentation as potential successors to atomic counterparts.

As the number of SIMS experiments involving polyatomic projectiles increased, so did the number of observations regarding cluster ion bombardment [6, 7]. The most recent observations have led to the identification of several important properties influencing the application of cluster ions to SIMS. Included among the properties are increased neutral and secondary ion yields and decreased physical and chemical sample damage. Together, the characteristics increase the number of molecules available for SIMS analysis and improve the overall sensitivity of the imaging modality. Accordingly, the objectives of this chapter are to introduce the unique mechanism for desorption during polyatomic bombardment, to identify the special

properties of cluster ions in SIMS, and to discuss the implications of these properties to sensitivity, lateral resolution, and depth resolution during the imaging modality. Using these properties, we will show how the improved performance of cluster ions in SIMS imaging can be used to characterize the chemical composition of various biological samples. The discussion is not meant to provide an exhaustive literature review of this very large subject, but is aimed toward illustrating the important strategic advantages associated with the cluster SIMS imaging approach.

4.2 Physics of Cluster SIMS

Molecular dynamics (MD) computer simulations have been recognized to provide valuable insight into the energetic ion bombardment of solids [11]. Consequently, the calculations will be used as a platform to discuss the differences between the atomic desorption event and the polyatomic desorption event. As a note, neutral atoms are used as the incident projectile in MD calculations, while ions are used as the incident projectile in SIMS experiments. Therefore, for the remainder of the chapter, projectiles used in MD simulations will be described in the neutral state, while projectiles used in SIMS will be described in the ion state. Despite the discrepancy, the physical phenomena in MD simulations are still representative of the desorption event in SIMS experiments.

An understanding of the atomic bombardment event is essential for a complete appreciation of the cluster desorption mechanism to be realized. Accordingly, a representative simulation of a typical trajectory of a 15-keV Ga normal incidence impact on an Ag solid crystal is shown in Fig. 4.1a [12, 13]. The atomistic motion within the Ag crystal can be described as a complicated game of billiards. Specifically, individual atoms collide with and transfer energy to other individual atoms. The cascade of substrate atoms is predominantly influenced by the trajectory of the projectile through the solid. The large incident energy and small cross section of Ga cause the atom to penetrate deep into the Ag crystal. Therefore, a large amount of the primary energy is deposited well below the solid surface. The dissipation of significant energy into the bulk causes substantial disruption of Ag atoms within the structure. Moreover, insufficient energy at the solid surface leads to the ineffective desorption of material. Hence, a large amount of the projectile energy is wasted in terms of providing useful SIMS information.

The issue of energy deposition into solids at depths efficient for material ejection and inefficient for the accumulation of sample damage is critical to the practical behavior of primary projectiles in SIMS. Polyatomic projectiles overcome the energy dissipation pitfalls observed during atomic bombardment by distributing its total incident energy over a number of constituent atoms. For example, each C atom in a 15-keV C₆₀ projectile has 250 eV of kinetic energy [7]. The energy per C atom is significantly greater than the C–C bond strength in C₆₀. As a result, the C₆₀ cluster dissociates into 60 separate 250-eV C atoms upon impact with the solid. Because each C atom has 250 eV of energy and initiates an individual cascade event, the

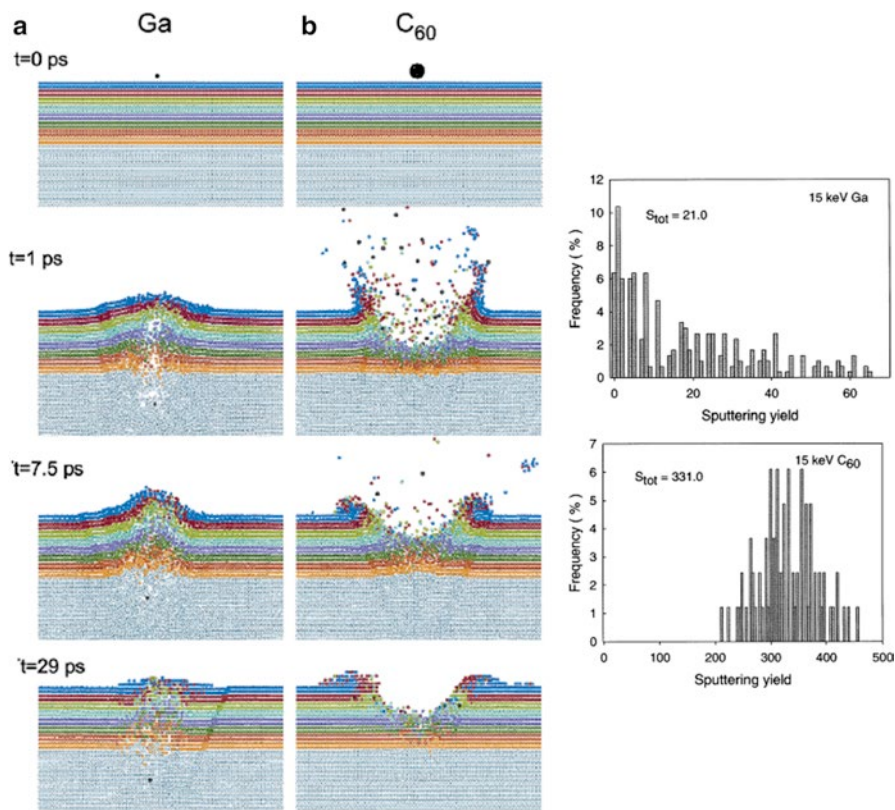


Fig. 4.1 Cross-sectional view of the temporal evolution of a typical collision event leading to the ejection of atoms due to 15-keV Ga (a) and 15-keV C₆₀ (b) bombardment of an Ag surface at normal incidence. The dimensions of the solid are $10 \times 10 \times 10 \text{ nm}^3$. The Ag atoms are colored by original layers in the solid. The projectiles are in black. The bar graphs are the relative frequency of impacts leading to a given sputter yield for 15 keV Ga (top) and 15 keV C₆₀ (bottom) (This figure is from Refs. [12, 13]). The calculations in this figure can be viewed as a movie file by visiting the website <http://www.chem.psu.edu/group/bjg/sputtering-animations>)

process for the deposition of energy into the substrate is considerably different than during 15-keV Ga bombardment. Specifically, the incident energy dissipates nearer the solid surface and over a larger surface area. Therefore, the motion of atoms within the substrate is also expected to be significantly different. A representative simulation of a typical trajectory of a 15-keV C₆₀ normal-incidence bombardment of a silver solid crystal is shown in Fig. 4.1b [12, 13]. The impact event itself resembles a meteor striking the earth. The motion of substrate material consequent to the event is similar to an organized expansion of a super-heated and super-dense gas from a pressurized nozzle. The cascade results in the formation of a significant crater within the solid and the occurrence of limited sample disruption outside this immediate region. Furthermore, the impact event is characterized by the large-scale

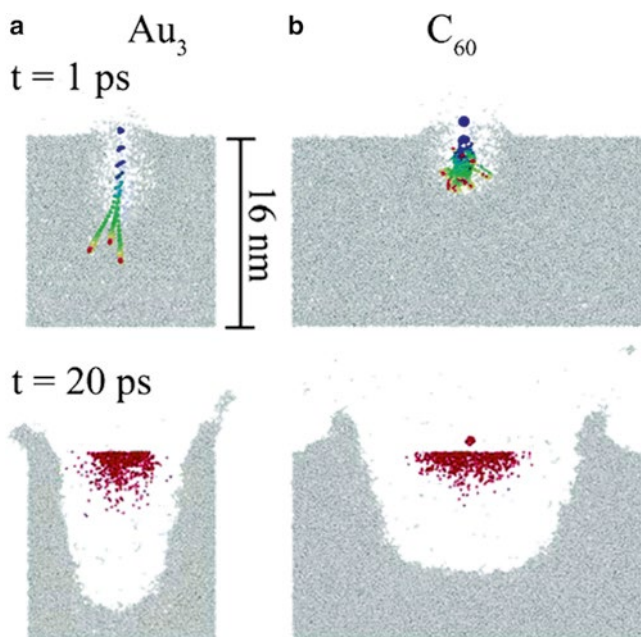


Fig. 4.2 Cross-sectional view of the temporal evolution of a typical collision event leading to the ejection of atoms due to 5-keV Au_3 (a) and 5-keV C_{60} (b) bombardment of an amorphous water surface at normal incidence. The dimensions of the solid are $29 \times 16 \times 16 \text{ nm}^3$. The *gray* atoms represent the water molecules. The snapshot at 1 ps contains a time-lapse overlay of the incident projectile motion within the solid. The snapshot at 20 ps displays the ejected atoms in *red* by original position in the solid (This figure is from Ref. [14]. The calculations in this figure can be viewed as a movie file by visiting the website <http://www.chem.psu.edu/group/bjg/sputtering-animations>)

ejection of material. In fact, the MD simulations illustrate a nonlinear enhancement of the number of Ag atoms removed for each incident C_{60} . That is, the yield for a 15-keV C_{60} impact is three times larger than the collective yield from 60 separate 250-eV C impacts. Thus, the polyatomic desorption event abandons linear cascade principles and enters the realm of the mesoscopic domain.

The unique mechanism for mesoscopic desorption is credited to the near-surface trajectories of the individual atoms of the cluster within the solid [14]. Specifically, the trajectories of the constituent atoms are influenced by two factors: the energy and mass per atom. Together, the factors determine the momentum of the constituent atoms and the mass-match of the constituent atoms with the substrate atoms. To illustrate this point, MD simulations of 5-keV Au_3 (Fig. 4.2a) and 5-keV C_{60} (Fig. 4.2b) normal-incident trajectories on amorphous water are considered [14]. The platform is significant since Au_3 and C_{60} are two commonly employed polyatomic projectiles. Moreover, the water sample consists of low-mass, weakly bound atoms comparable to organic materials. In general, the results of the Au_3 and C_{60} impact events on the water sample are similar. The motion of substrate material has

a mesoscale character, and a significant crater is formed within the solid. However, the trajectories of the incident projectiles within the solid giving rise to desorption are different. The motion of the constituent atoms in the Au_3 and C_{60} collision events are displayed in the time-lapse color portion of Fig. 4.2a, b, respectively. The different trajectories are attributed to each C atom in the 5-keV C_{60} particle having 83 eV of energy and a mass of 12 amu, while each Au atom in the 5-keV Au_3 particle has 1.7 keV of energy and a mass of 197 amu. Therefore, the Au atoms have a momentum 11 times larger than the C atoms and a mass that is much greater than the substrate atoms ($MW = 18$ amu). Consequently, the C atoms are promptly deflected by the substrate atoms upon impact, and the incident motion and excitation energy is confined to the near-surface region, whereas the Au atoms are slowly deflected by the much lighter substrate atoms, and the incident motion and excitation energy penetrate well beyond the near-surface region. Thus, the trajectories of the C atoms in the C_{60} collision event are more efficient for the near-surface deposition of energy into the solid. Thus, it is no surprise that the number of ice molecules removed in the C_{60} experiment ($Y = 1,644$) is larger than the number removed in the Au_3 experiment ($Y = 998$). Despite this modest difference, the constituent atoms in both the Au_3 and C_{60} clusters have significantly less momentum than a 15-keV Ga atomic projectile. Hence, polyatomic projectiles deposit their incident energy much more efficiently for providing useful SIMS information.

4.3 Properties of Cluster SIMS

The unique mechanism for desorption during polyatomic bombardment has led to an improved performance in SIMS. Experimental observations have identified several important properties when cluster ions are applied to SIMS. Specifically, when compared to atomic projectiles, polyatomic projectiles have been demonstrated to enhance secondary neutral and secondary ion yields—particularly in the case of large molecules—enhance surface sensitivity, reduce sample topography and inter-layer mixing, and make practical molecular depth profile and three-dimensional imaging experiments [6, 7]. Collectively, the behavior presents a unique opportunity for increased sensitivity, lateral resolution, and depth resolution during SIMS analysis. Therefore, this section will review the important characteristics of polyatomic projectiles in SIMS and comment on their implications to the imaging modality.

4.3.1 Enhanced Yields

The MD simulations shown in Fig. 4.1a, b indicate the yield of a 15-keV C_{60} impact ($Y = 331$) on a silver sample is 15 times larger than the yield for a 15-keV Ga impact ($Y = 21$) [12, 13]. The calculations are supported by the measurement of a similar yield increase for 15 keV C_{60}^+ over 15 keV Ga^+ on a polycrystalline Ag substrate using a quartz crystal microbalance (QCM) to determine the mass removed for each

impact [15]. Sputter-yield enhancements have also been observed for the polyatomic bombardment of organic-like materials. Specifically, QCM measurements have determined the number of molecular equivalents sputtered from an amorphous water–ice film using 20 keV C_{60}^+ ($Y=1,800$) to be 18 times larger than the number sputtered using 25 keV Au^+ ($Y=100$) [16]. Moreover, when 40 keV C_{60}^{3+} is employed, the absolute number of water molecules removed for each impact is increased to 10,000 [17]. Additional organic materials determined to experience large yield enhancements include polymethyl methacrylate (PMMA), polylactic acid (PLA), arachidic acid, benzene, phenylalanine, gramicidin S, and trehalose, to name a few [18–24]. Regardless of the sample, the amount of material removed for each cluster ion impact is significantly larger than the material removed for each atomic ion impact.

Similar to secondary neutral yields, secondary ion yields are enhanced during cluster projectile impact events [8–10, 20, 25, 26]. However, the increase observed for ions is not as straightforward to interpret as the increase observed for neutrals [6, 7]. Particularly, the extent of the secondary ion improvement is specific to the mass of the molecule being analyzed. For the case of molecules that weigh no more than 500 amu, polyatomic projectiles typically increase ion yields by a factor of 10–100 over atomic projectiles at comparable energies [20]. The observed ion enhancement is similar in magnitude to the observed neutral enhancement. Thus, the increase in ion yield is attributed to a corresponding increase in the neutral yield, and not an increase in ionization efficiency. This idea is supported by a series of experiments performed on a barium arachidate (MW=449 amu) multilayer structure prepared using Langmuir–Blodgett techniques [20]. The experiments use the known thickness of the structure to measure the number of incident projectiles required to remove the film using both Ga^+ and C_{60}^+ . From the information, the neutral yield and ion yield for Ga^+ and C_{60}^+ can be compared. The values indicate that the enhancement for C_{60}^+ over Ga^+ is a factor of 100 for both neutrals and ions. Therefore, the increase in secondary ion yield can be explained by an equivalent increase in the secondary neutral yield.

On the other hand, molecules weighing at least 500 amu typically experience a 100–1,000 fold increase in secondary ion yield when polyatomic projectiles are used [8, 25]. For some examples (Fig. 4.3a, b), such as the polymer PS-2000 (MW \approx 1,800 amu) and the peptide Gramicidin D (MW = 1,880 amu), a parent ion signal can only be observed if cluster projectiles are employed [8, 10]. The reason for larger enhancements at higher masses is not completely understood. However, a leading conjecture involves a larger propensity for polyatomic projectiles to “lift off” large, intact molecules while minimizing fragmentation. This proposition is supported by the MD simulations in Fig. 4.1a, b, which indicate that C_{60} has a higher probability of forming larger Ag clusters than Ga does [12, 13]. In addition to decreased fragmentation, another possible reason for the enhancement includes an improved environment for ionization under cluster bombardment [6, 7]. Experiments on amorphous ice films suggest that polyatomic projectiles are prodigious producers of protons in the impact region [27]. Thus, the ionization efficiency could potentially be increased through proton-attachment, chemical ionization of heavier, slower-moving molecules. Regardless of the scheme, polyatomic

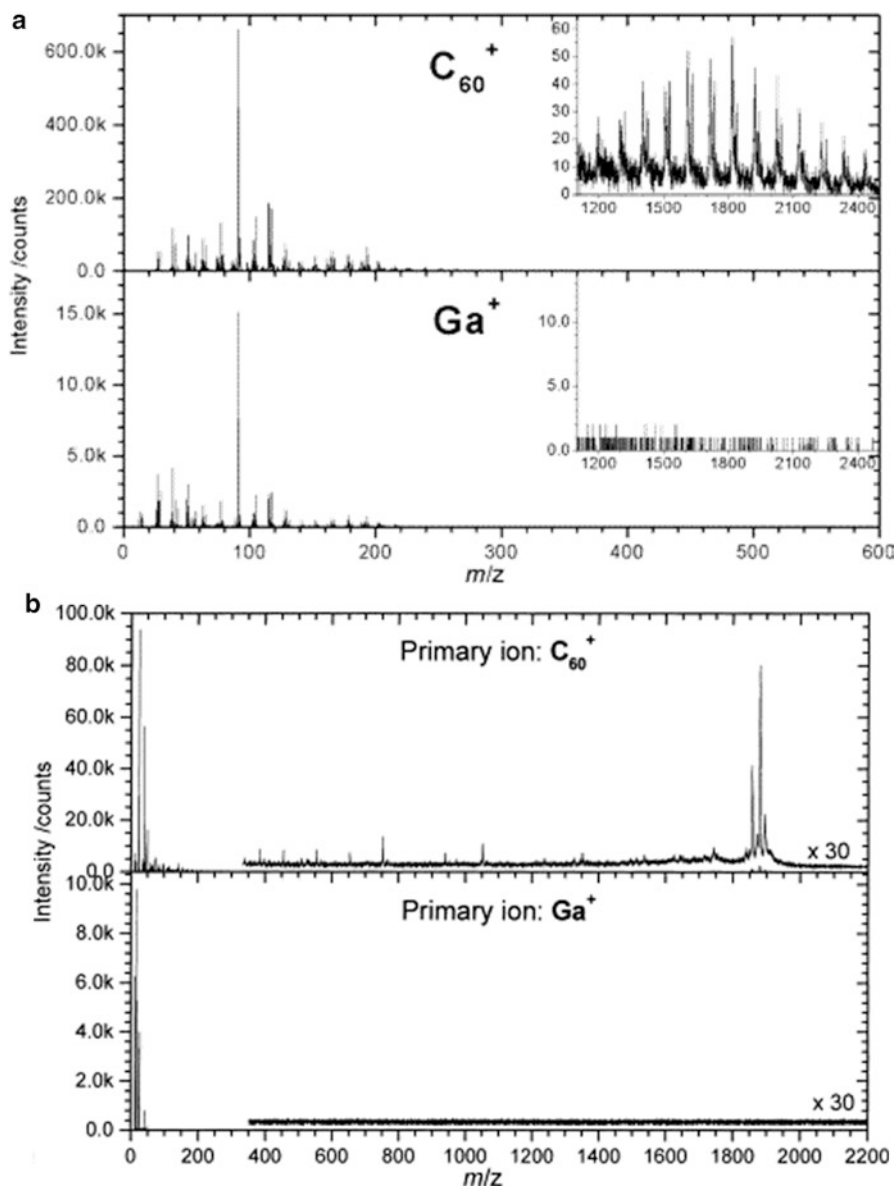


Fig. 4.3 (a) Positive SIMS spectrum of PS-200 using 10 keV Ga (*bottom*) and 10 keV C_{60} (*top*). (b) Negative SIMS spectrum of Gramicidin D using 15 keV Ga (*bottom*) and 15 keV C_{60} (*top*). All spectra acquired using the same primary ion fluence (From Refs. [8, 10])

projectiles have been demonstrated to considerably increase the sensitivity and extend the mass range of molecules in SIMS. These properties make available a new class of molecules, which includes polymers, peptides, proteins, and lipids, for detection during SIMS.

4.3.2 *Reduced Physical Damage*

The MD simulations in Fig. 4.1a, b provide valuable insight into the incidence of physical damage during SIMS [12, 13]. Specifically, the calculations indicate that C_{60} disrupts the sample bulk to a lesser extent than Ga does. That is, C_{60} appears to be more sensitive to the surface material than Ga does. In fact, surface sensitivity during projectile bombardment has been measured by observing the SIMS response of an Ag substrate that is covered with water–ice overlayers of various thicknesses and bombarded with 25 keV Au_{1-3}^+ and 20 keV C_{60}^+ [16]. The experiments indicate the amount of silver signal attenuation is greatest when the water–ice overlayer is interrogated with C_{60}^+ . Therefore, C_{60}^+ transfers the largest amount of its incident energy into the water–ice overlayer and has the highest surface sensitivity of the projectiles studied. The observation of enhanced surface sensitivity has the potential to reduce ion-beam–induced topography and interlayer mixing.

The incidence of reduced physical damage during polyatomic bombardment has significant implications to depth-profile experiments. Depth-profiling measurements are achieved by alternating between erosion cycles and SIMS acquisition cycles using a single ion beam. That is, the ion beam is operated in direct current (DC) mode to systematically etch material from a sample layer by layer and operated in pulsed mode to characterize the composition of the uncovered surfaces [6, 7]. For the individual layers to be resolved in the analysis, the ion beam must erode the sample without the occurrence of significant physical damage. Atomic projectiles do not meet these requirements unless considerable changes to the analytical strategy are made [28, 29]. These changes, which include low-energy primary ion bombardment (100–500 eV), glancing incident angles, and sample rotation, add substantial complexity to the measurements and eliminate the ability to acquire images [28, 29]. Conversely, polyatomic projectiles have been demonstrated in a number of instances to meet the depth-profile requirements without method modification.

The different behaviors of 15 keV Ga^+ and 15 keV C_{60}^+ during the controlled erosion of alternating nickel/chromium (Ni/Cr) layers in a multilayer structure are shown in Fig. 4.4 [28, 29]. The extent of interlayer mixing during the depth-profile experiment was determined by observing the response of the metal signal as a function of sample depth and calculating the interface distance between the alternating layers within the structure. In addition to the interface width, atomic force microscope (AFM) images of the eroded sample area were acquired to evaluate the ion-beam–induced sample topography. The measurements in Fig. 4.4 provide important insight into the depth resolution achieved during the Ga^+ and C_{60}^+ experiments. The depth profile using Ga^+ (bottom) does not resolve the individual Ni/Cr layers of the structure; the AFM measurement of the bombarded surface region (far right) indicates a 100-nm root-mean-square (rms) surface roughness. In contrast, the depth profile using C_{60}^+ (top) resolves the individual Ni/Cr layers with interface widths of 10 nm and the AFM measurement (left) determines a 2.5-nm rms surface roughness. Therefore, C_{60}^+ controllably erodes the Ni/Cr multilayer structure with a depth resolution of 10 nm, a value that is approaching the best resolution attained during low-energy, glancing incident, atomic projectile depth profiling. Overall, the improved

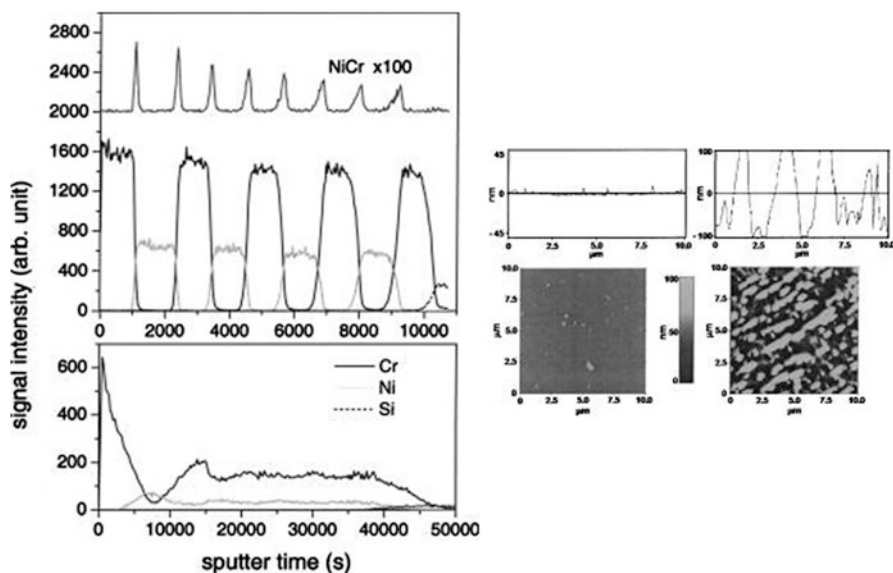


Fig. 4.4 The integrated metal atom signal response as a function of total sputter time for depth-profile experiments on a nine-layer Ni/Cr multilayer structure. The *top panel* shows the behavior of 15 keV C_{60} and the *bottom panel* shows the behavior of 15 keV Ga. The offset graphs are AFM images of the eroded region of the Ni/Cr structure using 15 keV C_{60} (*left*) and 15 keV Ga (*right*) (From Refs. [28, 29])

behavior of C_{60}^+ over Ga^+ during the Ni/Cr depth-profile experiments is attributed to reduced interlayer mixing and the absence of ion-beam-induced topography as a result of enhanced surface sensitivity.

Polyatomic projectiles have been employed to successfully depth-profile a number of multilayer structures [6, 7]. The ability to probe various materials without the incidence of significant physical damage has important implications to molecular depth profiling [6, 7]. To determine the potential for these experiments, the observation of reduced topography and interlayer mixing during cluster bombardment must be extended from atomic materials to organic materials. A platform for investigating the physical damage of organic materials during sample erosion is illustrated in Fig. 4.5 [22, 30, 31]. The platform involves a spin-coated, GGYR peptide-doped, sugar trehalose film on a silicon substrate. Figure 4.5a is an AFM image of the unbombarded trehalose surface, and Fig. 4.5b is an AFM image of the same surface after $1 \times 10^{14} \text{cm}^{-2}$ 20-keV C_{60}^+ bombardment. The AFM measurements indicate the rms surface roughness of the film before bombardment is 2.2 nm, while that after bombardment is 0.5 nm. Therefore, C_{60}^+ bombardment does not alter the surface topography of the trehalose film; however, this observation is not consistent for all materials [32]. In addition to limited topographical effects, the depth profile in Fig. 4.5c suggests the interface region of the trehalose molecules with the silicon substrate atoms during sample erosion is 10 nm. Thus, the physical structure of the trehalose film is maintained as a function of sample depth.

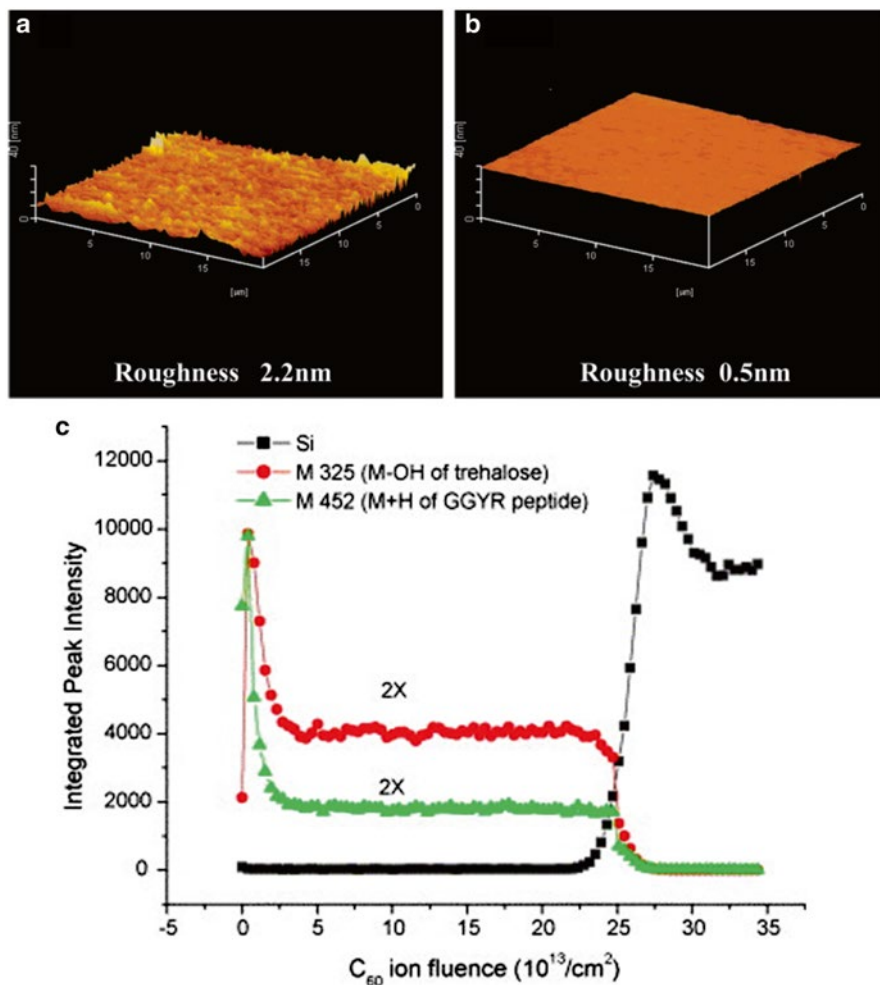


Fig. 4.5 AFM images of (a) an unbombarded sugar trehalose film surface and (b) a 1×10^{14} -cm⁻² C₆₀⁺ bombarded sugar trehalose film surface. The field of view is $20 \mu\text{m} \times 20 \mu\text{m}$. The labeled roughness corresponds to the rms values determined from statistical analysis of the entire image. (c) Depth-profile plot of secondary ion intensities of trehalose m/z 325 (red circle), GGYR peptide m/z 452 (green triangle), and silicon (black square) as a function of C₆₀⁺ ion fluence. The trehalose/ GGYR film is 350 nm thick (From Ref. [22])

4.3.3 Molecular Depth Profiling

SIMS experiments of organic materials using atomic projectiles have traditionally been limited by the accumulation of chemical damage at the solid surface [6, 7, 11]. The chemical damage is created by the ion-beam-induced fragmentation of molecules. After extended bombardment, fragmented molecules collect at the solid

surface and cover undamaged molecules. To avoid the loss of information, ion beam erosion of the solid is often limited to 1% of the surface molecules. This restriction, known as the static limit, considerably reduces the amount of material available for analysis. Consequently, the sensitivity and lateral resolution of the SIMS imaging modality are often inadequate for most organic and biological applications when atomic projectiles are used.

Polyatomic projectiles have the potential to overcome the static limit requirement. Collectively, large yields, enhanced surface sensitivity, low topography, and reduced interlayer mixing open the door to molecular depth-profile experiments. Molecular depth-profile experiments aim to systematically remove material from an organic solid layer by layer and expose a molecularly intact surface for SIMS characterization [6, 7]. The success of the experiment relies heavily on the ability to etch the sample without the accumulation of chemical damage. The large yields and high surface sensitivities characteristic of cluster bombardment severely confine the deposition of incident energy to the solid surface. Therefore, the bulk of the ion-beam fragmented molecules are sputtered during the impact event. Moreover, residual molecule damage remains near the surface and is easily removed by subsequent bombardment. Thus, polyatomic projectiles erode organic material at a rate that prevents the accumulation of significant chemical damage at the sample surface. In addition to reduced chemical damage, decreased topography and interlayer mixing allow for the organic material to be removed without a significant physical change to the underlying solid. Thus, the pieces are in place for successful molecular depth-profile experiments.

The advantages of cluster projectiles have been used to successfully depth-profile a number of molecules. Gillen et al. have routinely demonstrated the feasibility of the experiments using 5 keV SF_5^+ as a sputter projectile [3, 19, 33, 34]. An example from the research involves the controlled erosion of a polylactic acid (PLA) polymer film dosed with 5% drug molecule [19]. The depth-profile plots of secondary ion intensity versus SF_5^+ primary ion fluence for the PLA polymer, the drug molecules, and the silicon substrate are illustrated in Fig. 4.6c, d. The measurements are characterized by three distinct regions: an initial period of molecule signal fluctuation often referred to as the transient region of a depth-profile measurement; an extended steady-sputter-state region, where the ion intensities do not vary as a function of erosion time; and the complete disappearance of molecular signal at the silicon interface. Most notably, the steady sputter state indicates SF_5^+ can erode the material without the accumulation of significant chemical damage.

The idea of molecular stability during sample erosion has been extended to additional organic materials using C_{60}^+ as a sputter projectile by Winograd et al. [18, 20, 22, 30, 31, 35–37]. An example from the research uses a spin-coated, GGYR peptide-doped, sugar trehalose film as a platform [22, 30, 31]. A depth-profile plot of secondary ion intensity versus C_{60}^+ primary ion fluence for the trehalose molecule, the peptide molecule, and the silicon substrate is illustrated in Fig. 4.5c. Similar to the PLA polymer films, the trehalose signal and the peptide signal reach a steady sputter state before the silicon interface is reached. Furthermore, if the same film is eroded using 20-keV Au^+ , all molecular signals immediately disappear.

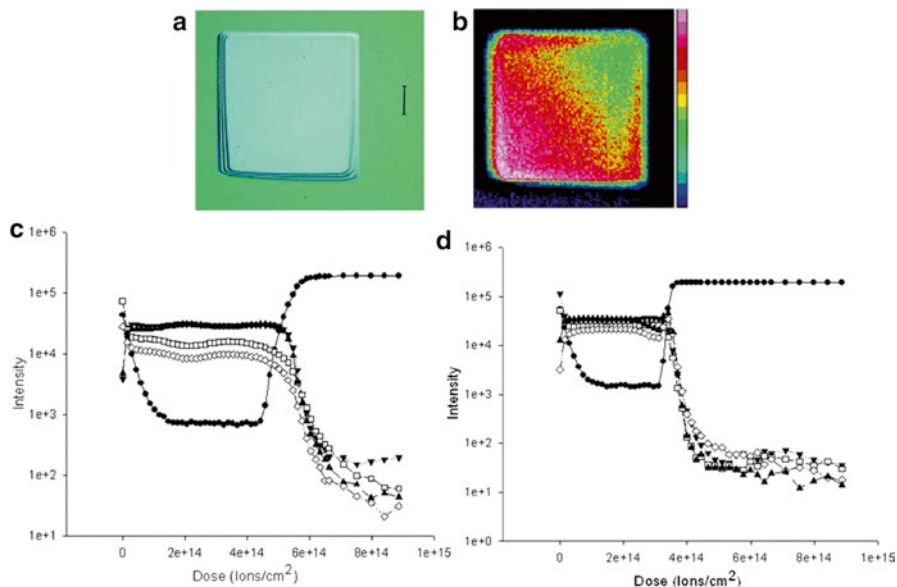


Fig. 4.6 (a) Optical micrograph of a typical sputter crater formed after bombarding a 560-nm-thick PLA film with 5 keV SF_5^+ . Scale bar represents 200 μm . (b) Si^+ molecule-specific SIMS image of a sputter crater formed after bombardment of a PLA film with SF_5^+ . (c) Secondary ion intensities as a function of increasing SF_5^+ primary ion dose for PLA films doped with 20% 4-acetamidophenol: (\blacktriangle) m/z 152, 4-acetamidophenol ($\text{M}+\text{H}$) $^+$; (\blacktriangledown) m/z 109, 4-acetamidophenol ($\text{M}+\text{H}-\text{COCH}_3$) $^+$; (\diamond) m/z 145, PLA fragment ($2n+\text{H}$) $^+$; (\square) m/z 128, PLA fragment ($2n-\text{O}$) $^+$; and (\cdot) m/z 28, Si^+ . (d) Secondary ion intensities as a function of increasing SF_5^+ primary ion dose for PLA films doped with 5% theophylline: (\blacktriangledown) m/z 128, PLA fragment ($2n-\text{O}$) $^+$; (\square) m/z 145, PLA fragment ($2n+\text{H}$) $^+$; (\diamond) m/z 165, theophylline ($\text{M}+\text{H}-\text{O}$) $^+$; (\blacktriangle) m/z 181, theophylline ($\text{M}+\text{H}$) $^+$; and (\cdot) m/z 28, Si^+ (From Ref. [19])

Consequent to the observations, a simple analytical model was developed to explain the basic response of molecular ion intensity as a function of primary ion fluence during the erosion process [22]. The molecular depth-profile model considers a number of parameters, including the molecule sputter yield, the damage cross section of the surface molecules, and the thickness of the surface layer altered by the projectile. Specifically, the model is described by the equation

$$\frac{dc_s}{df} = \frac{Y^{\text{tot}} c_b}{nd} - \frac{Y^{\text{tot}} c_s}{nd} - \sigma_d c_s$$

where c_s is the surface concentration of intact molecules, c_b is the bulk concentration of intact molecules, f is the primary ion fluence, Y^{tot} is the total molecule sputtering yield, n is the molecular density, d is the altered layer depth beneath the surface, and σ_d is the area of damage on the surface [22]. The first term in the equation describes the supply of undamaged molecules from the bulk to the surface during the erosion process, the second term describes the loss of intact molecules from the surface

during sputtering, and the third term describes the damage of intact molecules remaining at the surface. Collectively, the equation indicates favorable conditions for molecular depth profiling exist when the total sputter yield is large relative to the damage cross section and altered layer thickness. The conditions have repeatedly been observed in molecular depth-profile experiments using Au_3^+ , Bi_3^+ , and C_{60}^+ . Molecules that have been successfully eroded include trehalose, arachidic acid, PLA polymer, PMMA polymer, amino acids in ice, cholesterol, and phospholipids, to name a few [18–20, 22, 27, 31, 33, 37–42]. Currently, the experiments are limited to a depth resolution of 10 nm. Moreover, several molecules have been identified that do not respond well during the erosion process [32]. To overcome the challenges and better generalize the strategy, the experimental variables need to be optimized to best fit the conditions of the depth-profile model. Among the variables that can be varied, the incident energy and incident angle of the cluster projectile seem most promising. Accordingly, molecular depth-profile studies investigating the effect of the projectile incident energy and projectile incident angle are currently ongoing [42–44]. The experiments are expected to provide valuable information about the optimal incident projectile energy and the optimal incident projectile angle for the deposition of primary energy into a solid—an important factor in the determination of sputter yield and damage volume [45]. Thus, the research should identify the best conditions for molecular depth profiling and extend the usefulness of the analysis.

4.3.4 Implications to SIMS Imaging

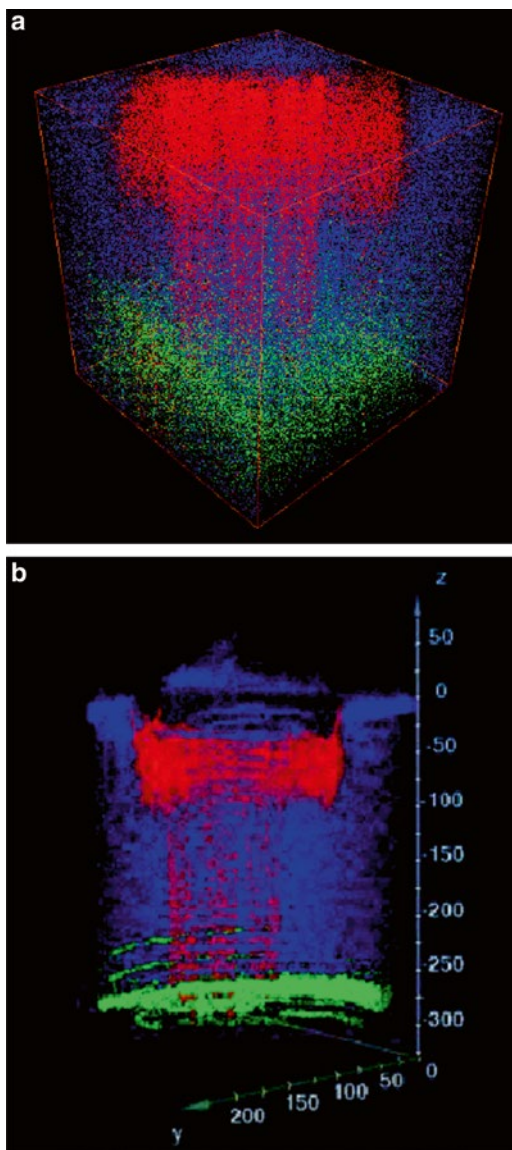
For a number of molecules, depth-profile experiments are feasible. The ability to eliminate the static limit requirement has major implications for the SIMS imaging of organic and biological materials [6, 7, 11]. SIMS images are acquired by rastering a focused ion beam across a sample surface and by collecting a mass spectrum at a sequence of surface positions. Software can be used to construct a two-dimensional (2D) image that displays ion intensity as a function of position (pixel) for a particular mass or a particular set of masses. In principle, the lateral resolution of the experiment is limited by the size of the ion beam, typically 100 nm. However, when atomic projectiles are employed, a fundamental flaw exists that causes the spatial resolution to be larger than the 100-nm beam size. The pitfall involves the accumulation of chemical damage after bombardment beyond the static limit [6, 7, 11]. Since only 1 % of the surface molecules are available for detection, the sensitivity of the SIMS measurement becomes inadequate as the pixel size approaches 100 nm × 100 nm. For instance, a molecular solid (1×10^{22} molecules/cm³) has approximately 5×10^4 surface molecules per 100-nm × 100-nm pixel. Taking into consideration the 1% static restriction, only 5×10^2 of the molecules are available for analysis. With a typical ionization efficiency of 1×10^{-4} , less than 1 molecule would be detected per 100-nm × 100-nm pixel [31]. In fact, the pixel size would

have to be increased to $1\ \mu\text{m} \times 1\ \mu\text{m}$ before 1 ion count is registered. Therefore, the lateral resolution of a static SIMS imaging experiment using atomic projectiles is fundamentally limited by sensitivity, and not by the size of the primary ion beam.

Polyatomic projectiles increase the number of molecules available for detection for samples more than one atomic layer thick. An increase in signal is attained by interrogating a pixel beyond the surface molecules and into the bulk of the solid [6, 7]. Considering the same molecular solid used in the previous example and the fact that cluster projectiles eliminate the static limit requirement, an increase in molecules over the same surface area can be achieved by changing the $100\text{-nm} \times 100\text{-nm}$ pixel to a $100\text{-nm} \times 100\text{-nm} \times 10\text{-nm}$ -deep voxel. The proposed three-dimensional voxel contains 1×10^6 molecules, each of which is available for analysis. With an ionization efficiency of 1×10^{-4} , 100 molecules would be detected within the $100\text{-nm} \times 100\text{-nm} \times 10\text{-nm}$ voxel. Furthermore, 10^4 molecules would be detected from a $1\text{-}\mu\text{m} \times 1\text{-}\mu\text{m} \times 10\text{-nm}$ voxel. Thus, SIMS imaging using cluster projectiles has a sensitivity many orders of magnitude greater than traditional static SIMS imaging using atomic projectiles. Moreover, the effective lateral resolution is considerably better when polyatomic projectiles are used.

In addition to an improved sensitivity, molecular depth-profile experiments have the potential to construct a three-dimensional (3D) chemical map of a multicomponent solid. A 3D SIMS image of a solid is assembled by acquiring retrospective images between erosion cycles during molecular depth-profile analysis. Following data acquisition, software is used to assemble the image series in a manner in which the ion intensity of a particular mass or a particular set of masses is displayed as a function of the lateral and depth distributions within the solid. Wucher et al. have developed a protocol for 3D SIMS image reconstruction [46]. The procedure was developed using a peptide-dosed, trehalose film patterned by bombardment with a focused 15-keV Ga^+ ion beam as a model. A high-resolution, image-series depth profile of this system was obtained using a focused, 40-keV C_{60}^+ ion beam. In addition to the SIMS images, complementary AFM images of the system were acquired before and after the depth profile. Together, the measurements were used to calibrate a depth scale for the construction of the 3D image. However, the calibration is complicated by highly nonuniform erosion rates within different regions of the solid. The dissimilar erosion rates were attributed to the heterogeneous distribution of various materials throughout the system. Therefore, the protocol mandates that an individual depth calibration must be performed for each pixel of the imaged area for a true 3D representation of the solid to be constructed. A depth scale for each pixel was calculated using the SIMS and AFM measurements, and a new sequence of 2D images was assembled to contain the correct mass spectra for a specific depth for a specific pixel. The new images were stacked in an array to produce a 3D image of the multicomponent solid. The 3D image results of the experiment before and after depth calibration are illustrated in Fig. 4.7a, b, respectively. The images clearly demonstrate the necessity of the depth-calibration protocol for the accurate composition of the solid to be visualized. Moreover, the images provide an exciting insight into the possibly vast information that may be available during 3-D SIMS imaging.

Fig. 4.7 (a) Uncalibrated 3D representation of a stack of sequential SIMS images with equidistant vertical spacing during a depth-profile experiment. *Red*, Ga^+ (m/z 69) signal from the initial Ga^+ bombardment; *blue*, $\text{M}+\text{H}^+$ (m/z 452) molecular ion signal of GGYR peptide in the trehalose overlayer; *green*, Si^+ (m/z 28) from the Si substrate. (b) Depth-calibrated 3D representation of solid composition as constructed from the AFM-SIMS measurements. Color representation is the same as in (a). The field of view is $200\ \mu\text{m} \times 280\ \mu\text{m}$ and the total eroded depth is 280 nm (From Ref. [46])



4.3.5 Comparison of Different Strategies

Before we introduce the various applications of cluster SIMS, a brief discussion for rationally selecting the optimal projectile for a specific experiment is appropriate [6, 7]. The assessment will emphasize the difference between $\text{Au}_3^+/\text{Bi}_3^+$ and C_{60}^+ projectiles in the SIMS. Other cluster projectiles, such as SF_5^+ , are not yet amendable to SIMS imaging due to the poor focusing characteristics and are omitted in the

discussion for simplicity. In general, C_{60}^+ provides enhanced yields and improved spectral quality as compared to Au_3^+/Bi_3^+ [8, 14, 17]. Furthermore, C_{60}^+ has a more surface-sensitive sampling depth and is more effective in molecular depth profiling [16, 22, 41]. The reason for these observations is attributed to each particle in the C_{60}^+ cluster having less energy than each particle in the Au_3^+/Bi_3^+ cluster. On the other hand, the imaging properties of Au_3^+/Bi_3^+ are currently better than C_{60}^+ [6, 7]. Specifically, Au_3^+/Bi_3^+ provides a brighter, more laterally defined beam size, although technical advances in C_{60}^+ focusing optics are rapidly narrowing the difference between these projectiles. In addition to smaller beam sizes, Au_3^+/Bi_3^+ implants metal atoms into the solid during the erosion process [41]. Heavy-metal implantation changes the chemical nature of the solid and may improve the ionization efficiency during SIMS [47]. The ramification of this occurrence has yet to be determined. Overall, the larger C_{60}^+ cluster is better for the acquisition of mass spectra and for molecular erosion, while the smaller Au_3^+/Bi_3^+ cluster is better for high-lateral-resolution imaging applications. Perhaps a compromise for optimal 3D SIMS imaging lies in dual-beam depth-profile analysis: C_{60}^+ is used for sample erosion and spectra acquisition, and Au_3^+/Bi_3^+ is used for imaging acquisition.

In addition to an assessment of projectile type, comparing cluster SIMS and its principal MS imaging complement—matrix-assisted laser desorption ionization (MALDI)—is useful when optimizing an MS strategy for a particular application [48]. Briefly, MALDI uses a matrix solution to segregate analyte molecules from a complex sample. The analyte-doped matrix crystals are ablated using a UV laser and the desorbed material is directed into a mass spectrometer. In general, MALDI provides high-quality mass spectra of large-molecular-weight molecules. The spectra are characterized by little fragmentation and a nearly unlimited mass range ($MW \geq 10^6$ amu). In addition, if a focused laser beam is used to acquire the spectra, an image of the sample can be constructed. MALDI imaging has been especially effective in the assay of large biological molecules, namely, peptides and proteins—an area SIMS imaging has been lacking. However, MALDI does not completely depict the vast range of molecules present within the sample. Specifically, the analysis is limited by little low-mass information ($\leq 1,000$), a chemical background attributed to the matrix, poor surface sensitivity (100 nm), and a lateral resolution restricted by the 10–100- μm laser beam size. The properties of cluster SIMS are an excellent complement to the MALDI pitfalls. Cluster SIMS excels in research where 0–1,000-amu target molecule mass ranges, chemically unmodified sample preparation, uppermost surface layer sensitivity, and submicrometer spatial resolution are important [6, 7, 11]. Thus, the applications of cluster SIMS emphasize research where these characteristics are essential.

4.4 Applications of Cluster SIMS

The special properties of cluster projectiles make the SIMS technique an exciting option for a number of applications in a number of research fields, including semiconductors, polymers, organic, combinatorial, chemistry, nanotechnology, and

biology. Perhaps the most intriguing application is the use of cluster SIMS as a chemical microscope in the discovery of new biology. Therefore, the remainder of this chapter will discuss the biological analyses made practical by the introduction of cluster projectiles to SIMS imaging, with particular attention paid to lipid molecules within biological tissue and biological single cells.

4.4.1 *Biological Tissue*

Recently, the distribution of lipid molecules in cellular membranes has become an increasingly important subject in the field of biology [49]. The interest has been prompted by the identification of lipids as key contributors in a number of cell processes, including signaling pathways, exocytosis, and endocytosis. The molecules have also been shown to play an important role in a variety of clinical diseases, namely Alzheimer's and Parkinson's. Thus, additional insight into lipid activity within cell membranes may lead to new findings in the areas of physiology, neurobiology, medicine, and pharmaceutical development.

A useful platform for investigating the function of lipids in intercellular activity is biological tissue [38, 50, 51]. Presently, strategies for *in vivo* analysis of these samples are problematic and provide little molecule specificity (i.e., magnetic resonance imaging, X-ray imaging, and microdialysis). However, procedures for dissecting, cryosecting, and preserving tissue while maintaining biological integrity for *ex vivo* analysis are better established. Unfortunately, common methods for *ex vivo* analysis offer an incomplete chemical representation of the samples. The strategies are flawed by the use of chemical labeling (i.e., fluorescence microscopy), insufficient molecule specificity (i.e., electron microscopy, Raman spectroscopy), and inadequate spatial resolution (i.e., MALDI imaging) [11, 50, 51]. In principle, SIMS is an ideal approach for overcoming these pitfalls. However, SIMS imaging using atomic projectiles of tissue samples has been limited by inadequate mass ranges (≤ 500 amu), poor sensitivities, and the identification of only a few lipid molecules, namely, the phosphatidylcholine headgroup (MW = 184 amu) [50, 51]. Collectively, these pitfalls considerably reduce the amount of biologically relevant information that can be learned.

By replacing atomic projectiles with cluster projectiles, one can considerably improve the effectiveness of the SIMS imaging modality [6, 7]. The broad repertoire of lipid molecules that is detected during cluster SIMS imaging of tissue is illustrated in Fig. 4.8a [50]. The figure is a sequence of negative SIMS molecule-specific images of a mouse brain section acquired using a focused 25-keV Au_3^+ ion beam and by scanning the sample target over a 9-mm \times 9-mm area. Most notably, the images identify numerous lipid species ranging in mass from 0–1,000 amu, including phosphate lipid headgroups, cholesterol, palmitate, oleate, stearate, phosphosulfatide, phosphatidylinositol, and phosphatidylcholine. Moreover, the images show a distinctive lateral distribution for each lipid present within the tissue. In fact, these distributions are so unambiguous that anatomic structures of the brain are

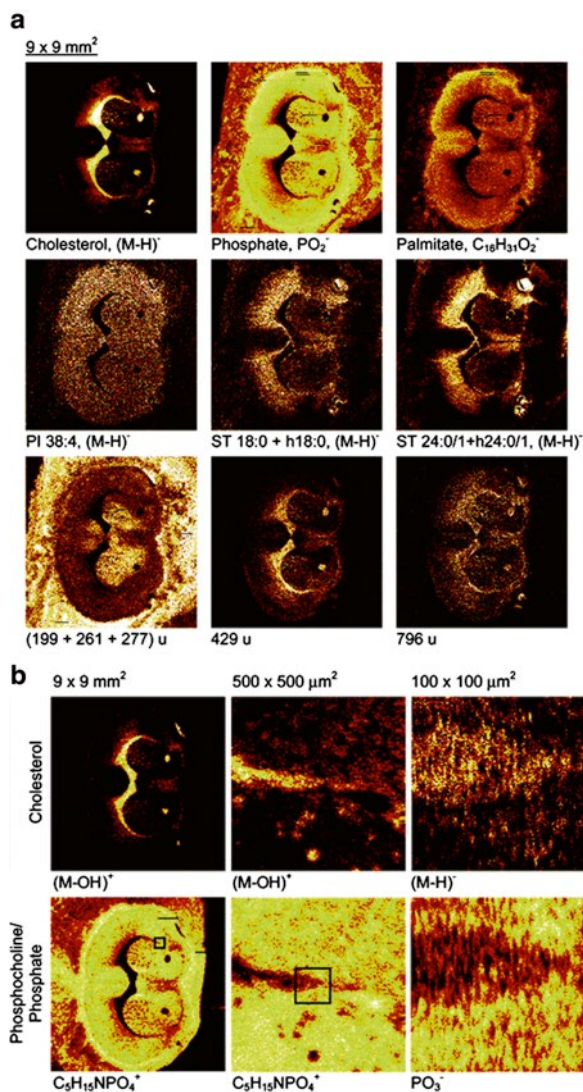


Fig. 4.8 (a) Negative SIMS molecule-specific images of a freeze-dried, coronal-sliced, mouse brain section acquired using 25 keV Au₃⁺. The specific ions, which include cholesterol (*m/z* 385), phosphosulfatide (ST, *m/z* 806, 822, 888, 890), phosphatidylinositol (PI, *m/z* 965), and unknowns, mapped in each image are indicated below the image itself. The field of view is 9 mm×9 mm. (b) Positive and negative SIMS images of the distribution of cholesterol and phosphocholine in a mouse brain section at different fields of view. The first column of images was a positive SIMS image at a 9-mm×9-mm field of view, the second column of images was a positive SIMS image at a 500-μm×500-μm field of view, and the third column of images was a negative SIMS image at a 100-μm×100-μm field of view. The effective lateral resolution in the images is 300 nm. The magnified images were obtained from the areas indicated by the *black squares* in the phosphocholine images (From Ref. [50])

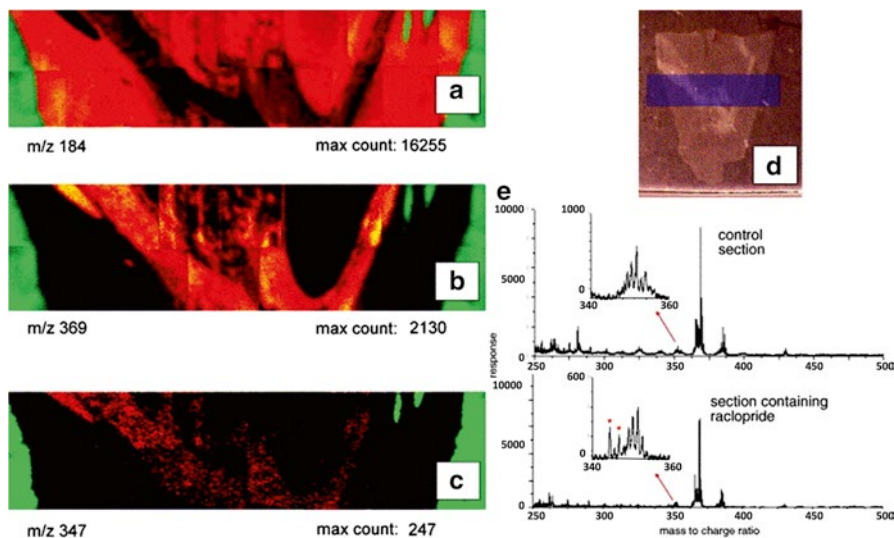


Fig. 4.9 Positive SIMS molecule-specific images of brain section taken from a rat treated *in vivo* with the drug raclopride acquired using 40 keV C_{60}^+ . The specific ions mapped include (a) phosphatidylcholine ($m/z=184$), (b) cholesterol ($m/z=369$), and (c) raclopride ($m/z=247$). In each image, the *green intensity* represents the substrate. The field of view is 1.6 mm \times 8 mm. (d) Optical image of the raclopride-treated, rat brain section. The *shaded region* illustrates the SIMS interrogated area. (e) Mass spectra illustrating the absence of the raclopride molecule in the control section and the presence of the raclopride molecule in the drug-treated section (From Ref. [39])

recognized. For instance, the images show a complementary localization between cholesterol and phosphocholine within the tissue. The heterogeneous distributions identify the cholesterol-enriched regions as white brain matter and the phosphocholine-enriched regions as gray matter. In addition, this occurrence of lipid heterogeneity is observed down to the micrometer scale (Fig. 4.8b).

An example of the improved detection levels attainable when cluster SIMS imaging is applied to tissue is shown in Fig. 4.9a–c [39]. The research uses a focused 40-keV C_{60}^+ ion beam to probe the drug raclopride—a dopamine uptake inhibitor—within a brain tissue section taken from a rat dosed *in vivo*. The positive SIMS molecule-specific images of the rat brain section are shown in Fig. 4.9a–c and are constructed by stitching together a number of analyses acquired at smaller fields of view. Figure 4.9a illustrates the distribution of phosphocholine (MW=184 amu) to identify the gray-matter region of the brain, Fig. 4.9b illustrates the distribution of cholesterol (MW=369 amu) to identify the white-matter region of the brain, and Fig. 4.9c illustrates the distribution of the raclopride drug (MW=247 amu). The images indicate that raclopride can be identified from within the treated brain section and that the drug is distributed within the white-matter region of the brain (Fig. 4.9e). Unfortunately, the spatial distribution of the drug within the sample does not completely agree with the known gray-matter location of the dopamine receptors. Although the basis for the inconsistency is unknown, potential explanations include

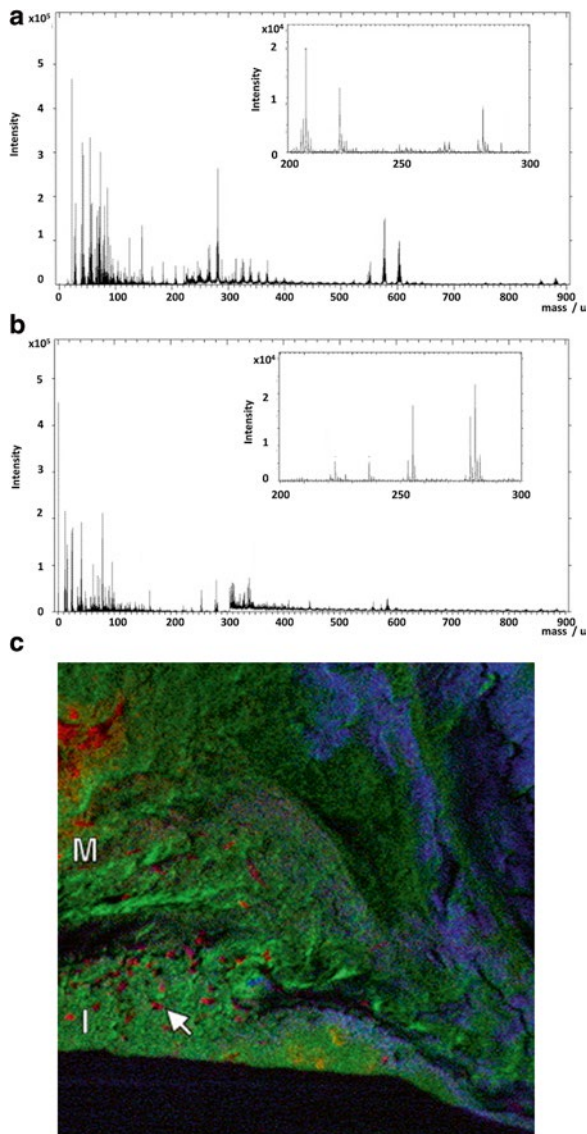
the redistribution of the drug after tissue preparation and the incidence of different ionization environments in the different regions of the tissue. Regardless of the issues, the experiment is encouraging since the raclopride-specific image demonstrates a two-part-per-million (ppm) detection level, a value that will improve even further once molecular depth profiling is applied—a feat that has already been deemed feasible on tissue homogenate when using 40 keV C_{60}^+ as erosion projectile [39].

Broad ranges of lipid molecules, distinct lipid localizations, micrometer lateral resolution, 1-ppm sensitivities, and molecular depth profiling make cluster SIMS imaging a powerful technique for the analysis of tissue. A real-life biological application utilizing the strategy is illustrated in Fig. 4.11 [52]. The application involves the interrogation of human atherosclerotic plaque to determine the role of lipids in the development of cardiovascular disease. In order to analyze the unhealthy artery, SIMS spectra of healthy rat aorta were acquired as a control using a Bi_3^+ ion beam (Fig. 4.10a, b). The spectra indicate that in a healthy artery, the lamellar tissue in the intima region (the innermost layer) is enriched in cholesterol, oxysterol, and diacylglycerols and that the smooth muscle tissue in the media region (the middle layer) is enriched in phosphocholine. Interestingly, the localization of lipids in the human atherosclerotic plaque shows a different distribution. Specifically, the SIMS molecule-specific image taken from the unhealthy artery shows an irregularly shaped distribution of cholesterol in the intima region and an irregularly located distribution of diacylglycerols in the media region. The unique lipid distributions suggest cholesterol and diacylglycerols play an important role in the development of cardiovascular disease. It is hypothesized that cholesterol may be an important ingredient in the apoptotic process leading to plaque formation and that diacylglycerol may be a mediator in the activation of this process. These hypotheses may be further developed by characterizing the role of these lipids in the formation of plaque at the cellular level.

4.4.2 *Biological Single Cells*

A useful platform for investigating lipids at the cellular level is biological single cells [6, 7]. For reasons similar to the analysis of tissue, SIMS is an excellent strategy for analyzing these samples. An example of the biological findings that can be learned from this partnership is illustrated in Fig. 4.11 [53]. The research involves the examination of highly curved lipids during cell conjugation. Specifically, the junction region between two conjoined cells contains a large number of fusion pores. The fusion pores, which are important in a number of cellular events, including sexual reproduction, exocytosis, and endocytosis, are hypothesized to be formed through the heterogeneous redistribution of lamellar and nonlamellar lipids throughout the membrane. Particularly, increased levels of nonlamellar or high-curvature lipids and decreased levels of lamellar or rigid lipids at the junction region are expected to provide the membranes with the necessary elasticity to form the highly curved intermediate structures required for conjugation (Fig. 4.11d). To examine

Fig. 4.10 (a) Positive and (b) negative SIMS spectra from a high-pressure, fresh-frozen, freeze-fractured, and freeze-dried rat aorta acquired using a Bi_3^+ ion beam. The spectra were used as reference in the analysis of human atherosclerotic plaque. (c) An overlay of positive SIMS molecule-specific images of human atherosclerotic plaque. The field of view is $500\ \mu\text{m} \times 500\ \mu\text{m}$. The *red signal* in the image represents cholesterol, the *green signal* represents phosphocholine, and the *blue signal* represents diacylglycerol. The section *M* indicates the media region of the tissue and the section *I* indicates the tunica intima region (From Ref. [52])



this hypothesis, SIMS molecule-specific images of mating *Tetrahymena* cells were acquired using a focused 15-keV In^+ ion beam. The images, which are illustrated in Fig. 4.11a, b, show a heterogeneous distribution of 2-aminoethylphosphonolipid (2-AEP; MW=126 amu), a nonlamellar lipid, and phosphocholine (PC; MW=184 amu), a lamellar lipid. Most notably, the fusion site between the two cells contains an elevated amount of the cone-shaped lipid 2-AEP and a depleted amount of cylindrical-shaped lipid PC (Fig. 4.11c). This observation supports the idea that

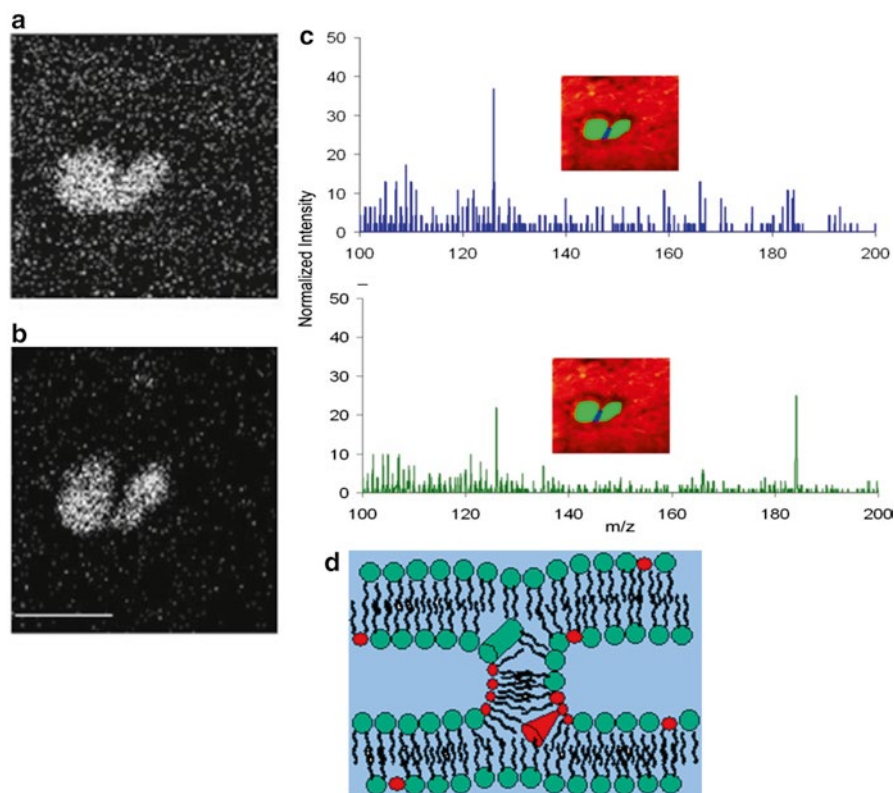


Fig. 4.11 (a–b) Positive SIMS molecule-specific images of mating, freeze-fractured, *Tetrahymena* cells acquired using a focused 15-keV In^+ ion beam. The specific ions are (a) 2-aminoethylphosphonolipid (2-AEP; MW = 126 amu), a nonlamellar lipid. The field of view is $100\ \mu\text{m} \times 100\ \mu\text{m}$, and (b) phosphocholine (PC; MW = 184 amu), a lamellar lipid. (c) Mass spectrum from the pixels along the conjugation junction (*top spectrum*) and from the cell body (*bottom spectrum*). (d) A schematic of the membrane fusion intermediate structure. The wavy lines depict the acyl tailgroups of the membrane phospholipids. The green circles are PC and red circles are 2-AEP, a cylinder-shaped lamellar lipid. The black circles represent the headgroup of 2-AEP, a cone-shaped nonlamellar lipid. Membrane fusion sites contain a large amount of cone-shaped lipids since these lipids fit well into contoured intermediate structures (From Ref. [53])

membrane fusion sites contain an increased concentration of nonlamellar lipids since cone-shaped lipids fit well into highly curved intermediate structures.

Future experiments using mating *Tetrahymena* aim to characterize the biological response that redistributes the lipids in preparation for the conjugation event. Unfortunately, single-cell SIMS imaging using atomic projectiles is limited to the identification of only a few lipid species. Moreover, these analyses are restricted to only the lipid molecules present within the uppermost layers of the exposed surface [54]. Therefore, a complete picture of the chemistry involved in the conjugation

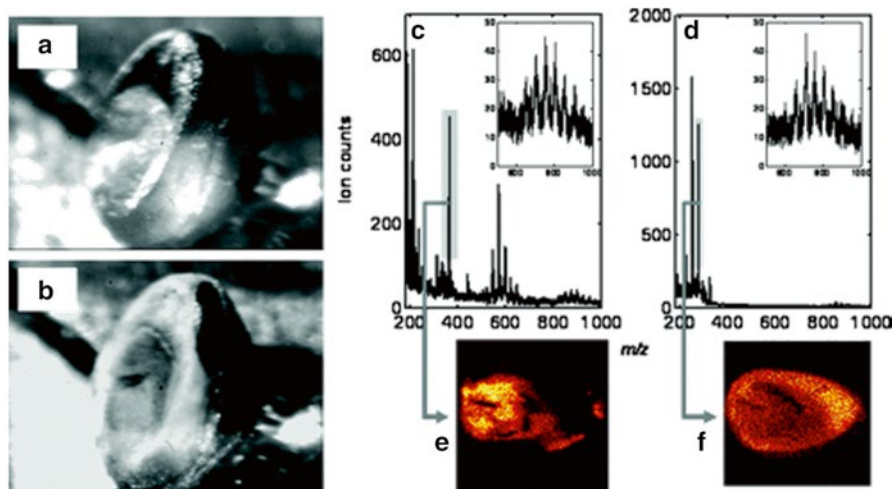


Fig. 4.12 (a–b) Optical micrograph of a *Xenopus laevis* oocyte cell mounted on copper tape for 40-keV C_{60}^+ SIMS analysis (a) before etching and (b) after etching. (c) Positive and (d) negative SIMS spectra from the oocyte cell after a 1×10^{15} C_{60}^+ /cm² etch. (e–f) SIMS molecule-specific images of the oocyte cell after a 1×10^{15} C_{60}^+ /cm² etch. The specific ions are (e) cholesterol (MW=369, positive SIMS) and oleic acid (MW=281, negative SIMS). The field of view is 1 mm \times 1 mm (From Ref. [54])

event cannot be drawn using the atomic SIMS imaging modality. Nevertheless, the desired information can be attained when using cluster projectiles as both an imaging projectile and an erosion projectile in 3D SIMS imaging. An experiment demonstrating the effectiveness of this strategy is shown in Figs. 4.12 and 4.13 [54]. The research involves the 3D molecule-specific SIMS imaging of a freeze-dried *Xenopus laevis* oocyte using a 40-keV C_{60}^+ ion beam (Fig. 4.12a, b). The positive and negative SIMS spectra shown in Fig. 4.12c, d demonstrate the wide array of lipid molecules that can be detected from the oocyte cell. Specifically, the lipid species identified in the spectra include phosphocholine (MW=58, 86, 166, 184 amu), cholesterol (MW=369 amu), lipid fatty acid side chains (MW: 540–720 amu), and glycosphingolipids (MW: 800–1,000 amu). In addition to lipid identification, the strategy is exciting with respect to lipid distribution as a function of the lateral and depth positions. Figure 4.13a–d display a 3D chemical representation of the oocyte cell. Of particular interest, the distribution of lipids within the image varies as a function of depth—with some species having a maximum intensity well below the sample surface. This observation is attributed to the removal of some molecules and the uncovering of others, suggesting that the 3D chemical integrity of the sample is maintained during erosion and the change in signal is representative of the molecular composition within the cell. Thus, 3D SIMS imaging using C_{60}^+ is an effective means for probing the chemistry of single cells in three dimensions.

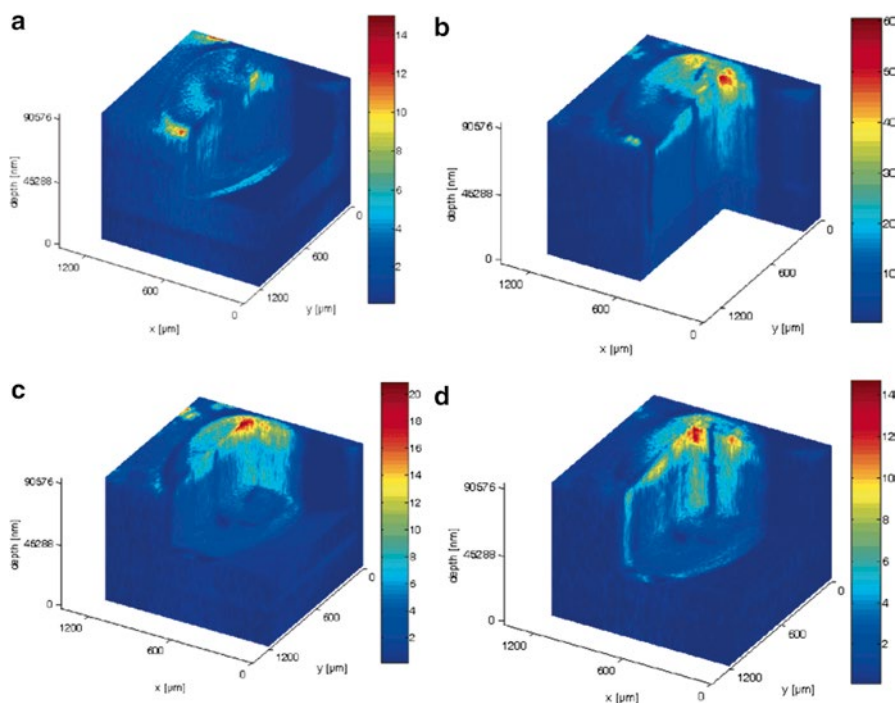


Fig. 4.13 (a–d) Three-dimensional positive SIMS image of a oocyte cell for (a) phosphocholine (MW = 58, 86, 166, and 184), (b) signal summed over m/z range 540–650, (c) signal summed over the m/z range 815–960, and (d) cholesterol peak (MW = 369) acquired using 40 keV C_{60}^+ . The 3-D representation is cut along two dimensions to display the third dimension. Color scale normalized for total counts per pixel for each mass. The field of view is 1 mm \times 1 mm and the depth is 100 μ m (From Ref. [54])

4.5 Future Directions of Cluster SIMS

The special properties of cluster projectiles have greatly improved the usefulness of the SIMS imaging modality [6, 7]. Therefore, the future use of the technique in the characterization of real-life biological samples, such as mating *Tetrahymena*, may lead to the discovery of new and exciting biology. While the prospects for these types of experiments are promising, several issues still remain that could possibly limit the technique, including sample preparation, instrument duty cycle, and ionization probability. While these challenges are not specific to the ion beam used, cluster projectiles may be useful in overcoming them.

Sample preparation is essential when acquiring meaningful SIMS images of single cells [55–57]. In order to prepare cells for in-vacuum analysis, the 3D integrity of the sample must be preserved in the solid state with micrometer precision. Common strategies for cell preservation include freeze-drying, freeze-etching, freeze-fracturing, chemical fixation, and sugar vitrification [55–59]. Although each of the strategies

has its advantages and its disadvantages, the “gold standard” is freeze-fracturing. Specifically, freeze-fracturing involves quenching hydrated cells for in-vacuum, cryogenic fracture and analysis. Unfortunately, the usefulness of the approach is limited by the absorption of an ice contaminant overlayer. Nevertheless, the overlayer can be removed with no damage to the underlying molecules using cluster ion bombardment [59]. Therefore, a good strategy for maintaining the 3D structure of biological samples while exposing an intact, meaningful surface for SIMS imaging involves combining freeze-fracture technology and cluster ion beams.

In addition to sample preparation, SIMS imaging of biological samples is also restricted by the instrumental duty cycle of axial time-of-flight (ToF) MS [60]. For example, to analyze each of the 10^8 molecules in a $1\text{-}\mu\text{m} \times 1\text{-}\mu\text{m} \times 10\text{-nm}$ voxel using a 10-pA ion beam with a 100-ns pulse width and a 10-kHz repetition rate, 10 s of instrumental time is required (assuming a sputter yield of 100). Therefore, it would take 182 h to acquire a $256\text{-voxel} \times 256\text{-voxel}$ image. However, by eliminating the pulsed nature of the ion beam, the same image can be acquired in only 11 min, or 10^3 less time. Specifically, a direct current (DC) ion beam is utilized by switching from an axial ToF geometry to an orthogonal ToF (oToF) geometry. In addition to rapid sampling, the proposed design allows for tandem MS/MS, collisional focusing, collisional cooling, and ion trapping when a series of quadrupoles (q) is placed between the sampling region and the ToF region. Therefore, the instrumental scheme extends the usefulness of the SIMS imaging modality—making the quadrupole-orthogonal ToF design with a cluster ion beam a possible SIMS instrument of the future.

Perhaps the most critical of the remaining issues is the ionization probability of the SIMS technique [61, 62]. Typically, only 1 in 10^4 desorbed molecules is an ion, meaning the majority of the signal is lost in the neutral fraction. Postionization of the neutral molecules using light sources is a common strategy for recovering the lost signal. To date, the postionization analysis has been limited by extensive fragmentation [61, 62]. The observation is attributed to photofragmentation and photodissociation of molecules sputtered with internally excited electronic states. The pitfall may be overcome by using cluster ion bombardment to desorb electronically cooled molecules [15, 63, 64]. Specifically, molecule cooling is achieved through large-scale collision events in the dense sputter plume. Therefore, by combining cluster projectiles with light sources, such as vacuum ultraviolet (VUV) radiation, mid-infrared (IR) light sources, and femtosecond visible light sources, postionization of neutral molecules may be possible without extensive fragmentation, improving the ionization probability and overall sensitivity of the experiments.

4.6 Summary

Recently, cluster projectiles have been introduced as replacements to atomic projectiles in the SIMS imaging modality. Since cluster ions have less energy per atom than atomic ions, a unique mechanism for desorption is utilized during bombardment. The mechanism, which is mesoscopic in nature, has led to the observation of

several important properties when cluster projectiles are applied to SIMS, including enhanced yields, reduced damage, and the feasibility of molecular depth profiling. Together, the properties considerably extend the usefulness of the SIMS imaging modality—especially when used to interrogate lipid molecules in biological tissue and biological single cells. Specifically, the analyses are characterized by extended mass ranges, improved detection levels, submicrometer lateral resolution, and 3D molecule-specific imaging. Moreover, the usefulness of the analyses can be improved further by combing cluster ion beams with freeze-fracture technology, qq-oToF instrumental design, and postionization using light sources.

Acknowledgments The authors acknowledge the National Institutes of Health under grant number EB002016-13, the National Science Foundation under grant number CHE-0555314, and the Department of Energy under grant number DE-FG02-06ER15803 for financial support.

References

1. Benninghoven A. *Zeitschrift for Physik A—Atoms Nuclei*. 1970;230:403–17.
2. Appelhans AD, Delmore JE. *Anal Chem*. 1989;61:1087–92.
3. Gillen G, Simons DS, Williams P. *Anal Chem*. 1990;62:2122–30.
4. Cornett DS, Lee TD, Mahoney JF. *Rapid Commun Mass Spectrom*. 1994;8:996–1000.
5. McMahon JM, Dookeran NN, Todd PJ. *J Am Soc Mass Spectrom*. 1995;6:1047–58.
6. Winograd N, Postawa Z, Cheng J, Szakal C, Kozole J, Garrison BJ. *Appl Surf Sci*. 2006;252:6836–43.
7. Winograd N. *Anal Chem*. 2005;77:142a–9.
8. Weibel D, Wong S, Lockyer N, Blenkinsopp P, Hill R, Vickerman JC. *Anal Chem*. 2003;75:1754–64.
9. Davies N, Weibel DE, Blenkinsopp P, Lockyer N, Hill R, Vickerman JC. *Appl Surf Sci*. 2003;203:223–7.
10. Wong SCC, Hill R, Blenkinsopp P, Lockyer NP, Weibel DE, Vickerman JC. *Appl Surf Sci*. 2003;203:219–22.
11. Vickerman JC, Briggs D, editors. *ToF-SIMS: surface analysis by mass spectrometry*. Manchester: SurfaceSpectra; 2001.
12. Postawa Z, Czerwinski B, Szewczyk M, Smiley EJ, Winograd N, Garrison BJ. *J Phys Chem B*. 2004;108:7831–8.
13. Postawa Z, Czerwinski B, Szewczyk M, Smiley EJ, Winograd N, Garrison BJ. *Anal Chem*. 2003;75:4402–7.
14. Russo MF, Garrison BJ. *Anal Chem*. 2006;78:7206–10.
15. Sun SX, Szakal C, Winograd N, Wucher A. *J Am Soc Mass Spectrom*. 2005;16:1677–86.
16. Szakal C, Kozole J, Russo MF, Garrison BJ, Winograd N. *Phys Rev Lett*. 2006;96:216104.
17. Russo MF, Szakal C, Kozole J, Winograd N, Garrison BJ. *Anal Chem*. 2007;79:4493–8.
18. Szakal C, Sun S, Wucher A, Winograd N. *Appl Surf Sci*. 2004;231–2:183–5.
19. Mahoney CM, Roberson SV, Gillen G. *Anal Chem*. 2004;76:3199–207.
20. Sostarecz AG, McQuaw CM, Wucher A, Winograd N. *Anal Chem*. 2004;76:6651–8.
21. Smiley EJ, Winograd N, Garrison BJ. *Anal Chem*. 2007;79:494–9.
22. Cheng J, Wucher A, Winograd N. *J Phys Chem B*. 2006;110:8329–36.
23. Van Stipdonk MJ, Harris RD, Schweikert EA. *Rapid Commun Mass Spectrom*. 1996;10:1987–91.
24. Tempez A, Schultz JA, Della-Negra S, Depauw J, Jacquet D, Novikov A, Lebeyec Y, Pautrat M, Caroff M, Ugarov M, Bensaoula H, Gonin M, Fuhrer K, Woods A. *Rapid Commun Mass Spectrom*. 2004;18:371–6.

25. Ostrowski SG, Szakal C, Kozole J, Roddy TP, Xu JY, Ewing AG, Winograd N. *Anal Chem.* 2006;78:973.
26. Xu JY, Szakal CW, Martin SE, Peterson BR, Wucher A, Winograd N. *J Am Chem Soc.* 2004;126:3902–9.
27. Conlan XA, Lockyer NP, Vickerman JC. *Rapid Commun Mass Spectrom.* 2006;20:1327–34.
28. Sun S, Szakal C, Roll T, Mazarov P, Wucher A, Winograd N. *Surf Interface Anal.* 2004;36:1367–72.
29. Sun S, Wucher A, Szakal C, Winograd N. *Appl Phys Lett.* 2004;84:5177–9.
30. Cheng J, Winograd N. *Appl Surf Sci.* 2006;252:6498–501.
31. Cheng J, Winograd N. *Anal Chem.* 2005;77:3651–9.
32. Shard AG, Brewer PJ, Green FM, Gilmore IS. *Surf Interface Anal.* 2007;39:294–8.
33. Mahoney CM, Fahey AJ, Gillen G. *Anal Chem.* 2007;79:828–36.
34. Wagner MS, Lenghaus K, Gillen G, Tarlov MJ. *Appl Surf Sci.* 2006;253:2603–10.
35. Wucher A, Sun S, Szakal C, Winograd N. *Appl Surf Sci.* 2004;231–2:68–71.
36. Sostarecz AG, Sun S, Szakal C, Wucher A, Winograd N. *Appl Surf Sci.* 2004;231–2:179–82.
37. Wucher A, Sun SX, Szakal C, Winograd N. *Anal Chem.* 2004;76:7234–42.
38. Touboul D, Kollmer F, Niehuis E, Brunelle A, Laprevote O. *J Am Soc Mass Spectrom.* 2005;16:1608–18.
39. Jones EA, Lockyer NP, Vickerman JC. *Int J Mass Spectrom.* 2007;260:146–57.
40. Kozole J, Szakal C, Kurczy M, Winograd N. *Appl Surf Sci.* 2006;252:6789–92.
41. Cheng J, Kozole J, Hengstebeck R, Winograd N. *J Am Soc Mass Spectrom.* 2007;18:406–12.
42. Fletcher JS, Conlan XA, Jones EA, Biddulph G, Lockyer NP, Vickerman JC. *Anal Chem.* 2006;78:1827–31.
43. Kozole J, Willingham D, Winograd N. *Appl Surf Sci.* 2007, submitted.
44. Cheng J, Wucher A, Winograd N. *Appl Surf Sci.* 2007, submitted.
45. Ryan KE, Smiley EJ, Garrison BJ. *Appl Surf Sci.* 2007, submitted.
46. Wucher A, Cheng J, Winograd N. *Anal Chem.* 2007;79:5529–39.
47. Marcus A, Winograd N. *Anal Chem.* 2006;78:141–8.
48. Karas M, Bahr U, Ingendoh A, Nordhoff E, Stahl B, Strupat K, Hillenkamp F. *Anal Chim Acta.* 1990;241:175–85.
49. Mukherjee S, Maxfield FR. *Annu Rev Cell Dev Biol.* 2004;20:839–66.
50. Sjoval P, Lausmaa J, Johansson B. *Anal Chem.* 2004;76:4271–8.
51. Sjoval P, Johansson B, Lausmaa J. *Appl Surf Sci.* 2006;252:6966–74.
52. Malmberg P, Borner K, Chen Y, Friberg P, Hagenhoff B, Mansson JE, Nygren H. *Biochim Biophys Acta-Mol Cell Biol L.* 2007;1771:185–95.
53. Ostrowski SG, Van Bell CT, Winograd N, Ewing AG. *Science.* 2004;305:71–3.
54. Fletcher JS, Lockyer NP, Vaidyanathan S, Vickerman JC. *Anal Chem.* 2007;79:2199–206.
55. Colliver TL, Brummel CL, Pacholski ML, Swaneck FD, Ewing AG, Winograd N. *Anal Chem.* 1997;69:2225–31.
56. Pacholski ML, Donald M, Cannon J, Ewing AG, Winograd NJ. *Am Chem Soc.* 1999;121:4716–7.
57. Roddy TP, Donald M, Cannon J, Meserole CA, Winograd N, Ewing AG. *Anal Chem.* 2002;74:4011–9.
58. Parry S, Winograd N. *Anal Chem.* 2005;77:7950–7.
59. Kurczy ME, Piehowski P, Parry S, Ewing AG, Winograd N. *Appl Surf Sci.* 2007, submitted.
60. Carado A, Kozole J, Passerelli M, Winograd N, Loboda A, Wingate J. *Appl Surf Sci.* 2007, submitted.
61. Vorsa V, Kono T, Willey KF, Winograd N. *J Phys Chem B.* 1999;103:7889–95.
62. Vorsa V, Willey KF, Winograd N. *Anal Chem.* 1999;71:574–81.
63. Wojciechowski IA, Kutliev U, Sun SX, Szakal C, Winograd N, Garrison BJ. *Appl Surf Sci.* 2004;231–2:72–7.
64. Wojciechowski IA, Sun SX, Szakal C, Winograd N, Garrison BJ. *J Phys Chem A.* 2004;108:2993–8.